ACS Catalysis

Research Article

Cite This: ACS Catal. 2020, 10, 672−682

pubs.acs.org/acscatalysis

Controlling Speciation during CO_2 Reduction on Cu-Alloy Electrodes

Xinyi Chen,[†,§] Danielle A. Henckel,[†,‡] Uzoma O. Nwabara,[‡,§] Yuanyuan Li,[∥] Anatoly I. Frenkel,[∥] Tim T. Fister,[⊥] Paul J. A. Kenis,[‡,§] and Andrew A. Gewirth*[,†,§]

[†]Department of Chemistry, University of Illinois at Urbana−Champaign, Urbana, Illinois 61801, United States

[§]International Institute for Carbon Neutral Energy Research (WPI-I2CNER), Kyushu University, Fukuoka, Fukuoka 819-0385, Japan

[‡]Department of Chemical & Biomolecular Engineering, University of Illinois at Urbana−Champaign, Urbana, Illinois 61801, United States

[∥]Department of Materials Science and Chemical Engineering, Stony Brook University, Stony Brook, New York 11794, United States

[⊥]Chemical Sciences and Engineering Division, Argonne National Laboratory, Argonne, Illinois 60439, United States

Supporting Information

ABSTRACT: Electrodeposition of Cu, Cu/Ag, and Cu/Sn alloy films by using 3,5-diamino-1,2,4-triazole (DAT) as an electrodeposition inhibitor yields a high surface area Cu-based catalyst. All three Cu-based electrodes exhibit high Faradaic efficiency (FE) of CO_2 reduction toward C_2H_4 production. The CuSn-DAT electrode exhibits the highest FE for CO (∼90% at −0.4 V) and C_2H_4 (∼60% at −0.8 V) production and high current density (∼−225 mA/cm^2 at −0.8 V). *In situ* surface enhanced Raman spectroscopy (SERS) studies in a flow cell obtained from the three Cu-based samples show a correlation between the decreased oxide content on the Cu surface, increased presence of CO, and increased activity for CO and C_2 production. The CuSn-DAT electrode has the lowest amount of Cu_2O and exhibits the highest activity, whereas the Cu-DAT electrode has an increasing Cu_2O content and exhibits lower activity as the potential is made negative. These results demonstrate that incorporation of different well-mixed alloy materials provides a way to tune CO_2 reduction speciation.

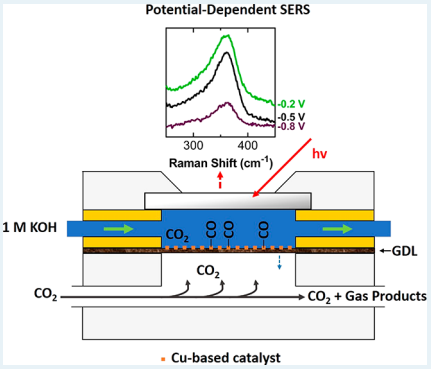

KEYWORDS: *CO_2 reduction, copper-alloy, ethylene, Raman, cupric oxide*

1. INTRODUCTION

As a result of fossil fuel combustion, annual CO_2 emissions have increased dramatically since the Industrial Revolution.[1] In 2019, the atmospheric CO_2 level exceeded 410 ppm and is expected to continue to rise.[2] The rise in CO_2 concentration is correlated with several environmental problems, such as global warming, rising sea levels, and more erratic weather patterns.[3−5] One way to reduce CO_2 content in the atmosphere is to utilize renewable energy sources such as solar energy, wind power, and geothermal energy. However, the intermittency of many renewable energy sources makes them unreliable and inappropriate for grid use without storage.[6,7] Electrochemical reduction of CO_2 may provide a promising solution to renewable energy intermittency and to the high atmospheric CO_2 levels, with CO_2 being converted to carbon monoxide, ethylene, ethanol, or other value-added chemicals.[8−19] By utilizing excess electricity generated from clean renewable energy sources, CO_2 reduction may provide a solution to the renewable energy intermittency problem through the storage of excess renewable electricity as chemical energy.[14,20] CO_2 reduction may also be utilized in direct atmospheric remediation schemes.[21,22]

Carbon monoxide is one of the most desired products of CO_2 reduction, and electroreduction of CO_2 to CO has been well-studied on Au and Ag nanoparticles (NPs).[16,17] The Faradaic efficiency (FE) for CO production on Au and Ag NPs can reach over 95% at high current densities. Formic acid or formate production is found to be dominant on the electrodes based on Sn,[23−26] Pb,[27] and Co[28] with ∼90% FE. Among all the metal catalysts, Cu is the only known metal that can convert CO_2 to hydrocarbons and oxygenates at appreciable levels during electroreduction as demonstrated in the pioneering work by Hori et al. in 1990s.[29−31] Although electroreducing CO_2 to hydrocarbons has promise, bulk Cu has very poor selectivity toward any specific product.[10] The hydrogen evolution reaction (HER) can also take place on the Cu surface, leading to loss of Faradaic efficiency for the desired product.

Intensive studies show that the selectivity for CO_2 electroreduction to one specific product can be enhanced by tuning the morphology,[12,13] alloying with other elements,[32−47]

Received: October 9, 2019
Revised: November 28, 2019
Published: December 2, 2019

DOI: 10.1021/acscatal.9b04368
ACS Catal. 2020, 10, 672−682

and controlling the oxidation state of Cu in Cu-based catalysts.[48−51] For example, Cu_2O or Cu_2O-derived Cu catalysts are reported to give better selectivity for C_2 products.[48−51] Previously, our group reported that electrodeposition of Cu and bimetallic CuAg using 3,5-diamino-1,2,4-triazole (DAT) as a deposition additive yielded rough and porous surface structures, both of which exhibit high selectivity for ethylene production (40−60% FE) during CO_2 electroreduction.[12,13] In addition, various Cu-based bimetallic catalysts have been developed to control speciation, such as phase-separated CuPd,[14] uniform AuCu NPs,[32] and a $Ag_{0.14}Cu_{0.86}$ alloy catalyst[33] to enhance the selectivity specifically for C_2 or C_1 products. The addition of Sn to Cu has been explored to control speciation during CO_2 reduction in configuration, such as Cu/SnO_2 core/shell NPs,[34] Sn-modified Cu foam,[35] a Sn/Cu(100) catalyst,[36] and CuSn nanowires.[44] However, most of these bimetallic CuSn catalysts only improve selectivity for C_1 products.[34−47]

Many laboratory-based CO_2 electroreduction measurements are performed in a CO_2 saturated $KHCO_3$ solution in an H-cell.[52−54] Several problems may be caused by the H-cell configuration, such as the depletion of dissolved CO_2, change of surface pH over time, limitations in available pH values at the electrode, and poisoning of the surface by products. Mostly due to mass transport limitations, H-cells also exhibit relatively low current density (~20 mA/cm^2) for CO_2 reduction, a value inconsistent with industrial requirements. Compared to the H-cell setup, the alkaline flow electrolyzer provides more control of surface composition and exhibits substantially higher current densities (up to 1 A/cm^2) with increased durability.[15] The ability to continually remove products away from the surface and to operate in a more alkaline environment are benefits that make this configuration desirable.

A number of studies examining CO_2 reduction on Cu by using *in situ* vibrational spectroscopic techniques have been reported.[52−58] These studies are performed with stationary electrolyte, leading to issues similar to those encountered in the H-cell studies described above. For example, a recent *in situ* Raman study evaluated potential-dependent surface speciation but in stagnant $KHCO_3$ electrolyte.[59] It is desirable to obtain spectroscopic insight into surface speciation during high current CO_2 reduction in more alkaline electrolyte, since this configuration is more industrially relevant. It is also desirable to obtain *in situ* spectroscopic insight into the change in surface oxidation state during CO_2 reduction on Cu with the flowing electrolyte.

In this study, we compare the relative selectivity of CO_2 electroreduction among three different samples based on Cu alone, a CuAg alloy, and a CuSn alloy. The samples are prepared using an electrodeposition protocol that yields high surface area catalysts featuring well-mixed, low alloy content materials. *In situ* surface enhanced Raman spectroscopy (SERS) is utilized to understand the observed differences in catalytic behavior relative to the formation of CO and C_2 products attendant the three Cu-based systems (Cu-DAT, CuAg-DAT, and CuSn-DAT). Our data indicates the reduction of CO_2 to CO is affected by the degree of surface oxidation and limited by the available Cu sites on the surface. The addition of Sn to Cu, and to a lesser extent Ag, is shown to diminish the amount of Cu_2O on the electrode surface, leading to a higher concentration of adsorbed CO and attendant greater FE for CO and C_2 product formation.

2. EXPERIMENTAL SECTION

2.1. Preparation of Catalysts. All samples are comprised of a carbon paper-based gas diffusion layer (GDL) substrate (Sigracet 35 BC, Ion Power Inc.) on which a catalyst was electrodeposited. The plating baths for CuSn-DAT and CuSn-control were made from 10 mM $CuSO_4$, 10 mM $SnSO_4$, and 0.5 M H_2SO_4 with or without 1 mM 3,5-diamino-1,2,4-triazole (DAT). The Cu-DAT sample was prepared from 0.1 M $CuSO_4$ and 10 mM DAT at pH 1.5 adjusted by H_2SO_4, as described previously.[12] The CuAg-DAT sample was prepared from 10 mM $CuSO_4$, 0.1 mM Ag_2SO_4, and 1 mM DAT at pH 1.5 adjusted by H_2SO_4. This preparation is slightly different from that reported previously[13] and was chosen to maintain a constant [Cu^{2+}] between the different plating baths. All the chemicals were obtained from Sigma-Aldrich. Galvanostatic electrodeposition on the GDL at a constant current density of −4 mA/cm^2 was performed until a final deposition charge of 2 C/cm^2 was reached to generate the four samples with identical loading. Before electrodeposition, the GDL was pretreated by sputtering 10 nm of Cu using an AJA Orion-8 Magnetron Sputtering System. Pt was used as the counter electrode, which was separated from the working electrode by an ion exchange membrane (Fumatech FAP-375-PP) to prevent DAT from being oxidized at the counter electrode. A "leakless" Ag/AgCl (eDAQ) electrode was used as the reference electrode.

2.2. Characterization of Materials. Scanning electron microscopy (SEM) images were obtained utilizing a JEOL 7000F Analytical SEM. The amount of electrodeposited Cu and Sn was measured using inductively coupled plasma optical emission spectrometry (ICP-OES; PerkinElmer 2000 DV optical emission spectrometer). X-ray diffraction (XRD) patterns were obtained by using a PANalytical Phillips X'pert MRD system #2. X-ray photoelectron spectroscopy (XPS) was performed with a Physical Electronic PHI 5400 instrument. Pb underpotential deposition (UPD) was used to determine the electroactive surface area of each sample.[60]

An X-ray absorption fine structure (XAFS) experiment was performed at the sector 9 beamline at the Advanced Photon Source at Argonne National Laboratory utilizing a beam cross section of 2.6 mm (horizontally) × 0.75 mm (vertically). Samples were studied *ex situ* by layering 12 sheets of carbon paper onto which the CuSn films had been electrodeposited. Measurements for both Cu and Sn were recorded in transmission mode using a double-crystal Si (111) monochromator at 50% detuning. The ion chamber detector for Cu was filled with a mixture of He/N_2, and the ion chamber detector for Sn was filled with Ar.

2.3. CO_2 Electroreduction in a Flow Reactor. Electroreduction experiments and product analysis were conducted in a flow reactor setup described previously.[15,16] A mass flow controller (Smart Trak 2, Sierra Instruments) was used to flow CO_2 gas (S.J. Smith Welding Supply) at a flow rate of 7 standard cubic centimeters per minute (SCCM) over the cathode GDL. A syringe pump (PHD 2000, Harvard Apparatus) was used to pump 1 M KOH at a constant flow rate of 0.2 or 0.5 mL min^{-1}. The CO_2 electroreduction activity for all catalysts was measured by controlling the cathode potential with respect to a Ag/AgCl electrode (3 mol kg^{-1} KCl, RE-5B, BASi) using an Autolab PGSTAT-30, EcoChemie potentiostat in the potentiostatic electrolysis mode. All cathode potentials were converted to the reversible hydrogen electrode (RHE) by using the Nernst equation: E (vs RHE) = E (vs Ag/

DOI: 10.1021/acscatal.9b04368
ACS Catal. 2020, 10, 672−682

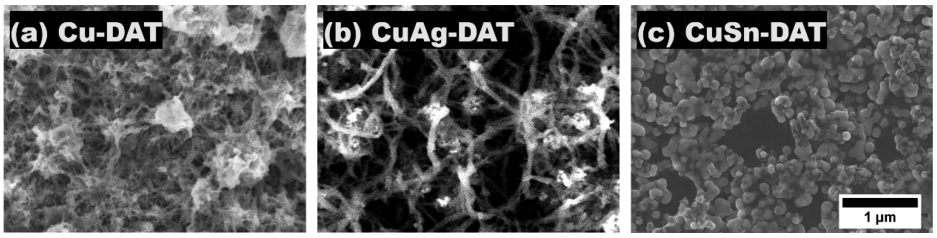

Figure 1. SEM images obtained from (a) Cu-DAT, (b) CuAg-DAT, and (c) CuSn-DAT samples electrodeposited on a GDL. All samples are shown at the same magnification.

AgCl) + 0.209 V + 0.0591 V × pH. IrO_2 with a loading of 2 mg/cm^2 on the GDL was used as the counter electrode.[16]

Three minutes after the potential was applied, the gaseous product stream was sampled automatically and diverted for analysis in a gas chromatograph (Thermo Finnigan Trace GC) equipped with both a thermal conductivity detector (TCD) and a flame ionization detector (FID). The exit electrolyte containing liquid products was collected and analyzed in an Agilent VNS750NB NMR spectrometer using a ^{1}H NMR technique described previously.[15] Dimethyl sulfoxide (DMSO) was used as an internal standard.

2.4. *In Situ* Electrochemical Raman Measurements. *In situ* Raman measurements were carried out by utilizing a spectro-electrochemical flow cell (Figure S4). A 2.0 mm thick polyether ether ketone (PEEK) spacer with a 0.5 × 2 cm hole was placed between a quartz window and the cathode GDL. For each *in situ* Raman measurement, the Raman spectrum was accumulated by 30 acquisitions (1 s per acquisition). A syringe pump (PHD 2000, Harvard Apparatus) was used to pump 1 M KOH at a constant flow rate of 1.0 mL min^{-1} over the GDL. CO_2 gas was introduced to the back of the GDL in a stainless-steel chamber at a flow rate of 7 SCCM controlled by a mass flow controller (Smart Trak 2, Sierra Instruments). For control trials using 1 M KOH electrolyte without CO_2, saturated $Ca(OH)_2$ (99.995% trace metals basis, Aldrich) was added to remove atmospheric CO_2 as insoluble $CaCO_3$ solid. Argon gas was introduced to the back of the GDL at a flow rate of 7 SCCM. Working electrodes were formed from Cu-DAT, CuAg-DAT, or CuSn-DAT electrodeposited on a GDL. Potentials were applied (in potential holds) with respect to a Ag/AgCl reference electrode (3 mol kg^{-1} KCl, RE-5B, BASi) and reported with respect to RHE. To be consistent with the electrolysis measurements, Raman spectra were obtained 3 min after the potential was initially applied. Potential-dependent spectra were obtained between −0.1 and −0.8 V vs RHE, except for the Cu-DAT and CuAg-DAT samples where substantial gas evolution precluded spectra at potentials more negative than −0.6 V. Airbrushed IrO_2 on a GDL placed in front of the cathode GDL was used as the counter electrode.

3. RESULTS

3.1. Characterization of CuSn Films. Figure 1a,b shows SEM images obtained from the Cu and bimetallic CuAg samples electrodeposited on a GDL with DAT. Both Cu-DAT and CuAg-DAT exhibit a wire-like structure, consistent with prior reports.[12,13] Figures 1c and S1a show SEM images obtained from bimetallic CuSn films electrodeposited on a GDL with and without DAT present in the plating bath, respectively. Both the CuSn-DAT and CuSn-control samples exhibit a series of circular particles, but the particles are approximately a factor of 2 smaller in diameter in the CuSn-DAT sample, compared to the CuSn-control. This result is consistent with prior work showing that the presence of the DAT inhibitor leads to smaller particles, likely because of increased nucleation density during deposition.[12] The atomic % of Sn (as measured by ICP) in the CuSn-DAT and CuSn-control samples is 8.3% and 15.2%, respectively. In comparison to films deposited either from Cu alone or CuAg, the CuSn films are less filamentous and exhibit a denser structure.

Pb UPD was utilized to determine the electroactive surface area of each sample, and the integrated Pb_{UPD} charge values are listed in Table S1.[60,61] The smaller Pb_{UPD} charge of CuSn-control shows that CuSn-control has a smaller electroactive surface area compared to CuSn-DAT. This result is expected due to the larger circular particles for the CuSn-control observed in the SEM. Cu-DAT and CuAg-DAT, which both have the wire surface structure, exhibit an electroactive surface area ∼1.7 times larger than the CuSn-DAT. The surface area for all the electrodeposited Cu samples is some 35−85 times larger than the GDL substrate with sputtered Cu alone.

Since Sn-alloying using our electrochemical method is new, Cu K-edge and Sn K-edge XAFS spectra (Figure 2) were measured to understand the Cu and Sn local bonding environments in the CuSn-DAT sample. As shown in Figure 2a,c, the Cu K edge X-ray absorption near edge structure (XANES) and extended XAFS (EXAFS) spectra of the CuSn-DAT sample are similar to those of Cu foil, suggesting the metallic nature of Cu in CuSn-DAT and bulk Cu-like local structure for Cu species. On the other hand, the Sn K edge spectra of the CuSn-DAT sample are different from those of Sn

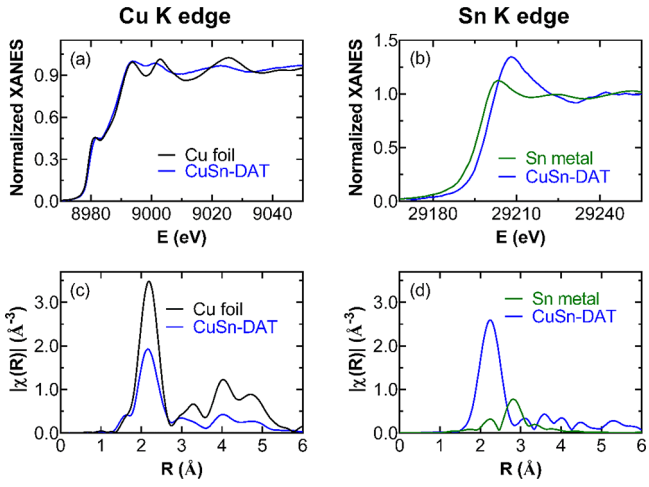

Figure 2. XAFS spectra of the Cu foil, Sn metal, and CuSn-DAT: (a) Cu K edge and (b) Sn K edge normalized XANES spectra and Fourier transform magnitudes of the k^2-weighted (c) Cu K edge and (d) Sn K edge EXAFS spectra.

DOI: 10.1021/acscatal.9b04368
ACS Catal. 2020, 10, 672−682

metal. In the near edge region (Figure 2b), the absorption edge energy of CuSn-DAT shifts to a higher value compared to that of Sn metal, and the white line intensity (at about 29208 eV) is higher than that in the Sn metal spectrum. These differences suggest the electronic properties of Sn in the CuSn-DAT are strongly modified by local environments, specifically, some degree of charge transfer from Sn to Cu. This charge transfer was also observed in prior work.[62]

In R space (Figure 2d), the EXAFS spectrum of Sn metal is dominated by a peak at about 2.8 Å due to the Sn−Sn contribution, while the spectra obtained from the CuSn-DAT sample shows a distinct peak at about 2.2 Å, suggesting again a different Sn local environment in the CuSn-DAT sample compared to Sn metal. Instead of neighboring Sn atoms, in CuSn-DAT, Sn could be predominantly coordinated by Cu atoms as implied by the spectral similarity between k-space EXAFS of the Sn edge of the sample and the Cu edge of the Cu foil (Figure S2).

To confirm the hypothesis of Sn mixing with Cu and to obtain quantitative local structure information, EXAFS data were analyzed. For the Sn K edge data analysis, the fitting model includes one path: Sn−Cu; for the Cu K edge data analysis, the fitting model includes two paths: Cu−Cu and Cu−Sn. The Cu K edge and Sn K edge data for each sample were fitted concurrently with several constraints applied: the bond distances and the disorder factors of the heterometallic bonds were constrained to be equal: R(Sn−Cu) = R(Cu−Sn), σ^2(Sn−Cu) = σ^2(Cu−Sn). The same energy shift variable was used for the Cu−Cu and Cu−Sn contributions. For Sn K edge data, the fitting k range is 2.0−11.0 Å^{-1} and the fitting R range is 1.8−2.8 Å; the amplitude reduction factor (S_0^2 = 1.1 ± 0.1) was obtained by fitting the Sn foil spectrum. For Cu K edge data, the fitting k range is 2.0−12.0 Å^{-1} and the fitting R range is 1.6−2.7 Å; S_0^2 (0.89 ± 0.05) was obtained by fitting the Cu foil spectrum. The best fitting results are summarized in Table 1, and the comparison between the experimental and fitted spectra are plotted in Figure S3.

Table 1. Values of Structural Parameters for the Near Coordination Shells of Cu and Sn Atoms in Cu Foil, Sn Metal, and CuSn-DAT Samples

samples	path	N	R (Å)	σ^2 (Å^2)
Cu foil	Cu−Cu	12	2.540 ± 0.003	0.0087 ± 0.0005
Sn metal	Sn−Sn	4	3.000 ± 0.006	0.0088 ± 0.0005
	Sn−Sn	2	3.11 ± 0.05	0.020 ± 0.007
CuSn-DAT	Sn−Cu	11.6 ± 1.5	2.65 ± 0.02	0.009 ± 0.004
	Cu−Cu	8.4 ± 0.4	2.55 ± 0.01	0.011 ± 0.003
	Cu−Sn	0.6 ± 0.3	2.65 ± 0.02	0.009 ± 0.004

As shown in Table 1, the average coordination number (N) for Cu−Cu in the CuSn-DAT is approximately 8.4. There is a small contribution from Cu−Sn, indicating that Cu is surrounded predominantly by Cu atoms. This observation is reasonable, considering the low weight percent of Sn in the CuSn-DAT. For CuSn-DAT, the total coordination number of Cu−metal (Cu−Cu and Cu−Sn) is 9.0 ± 0.5, which is smaller than that found in Cu foil.[12] A possible explanation for this discrepancy is the granularity of the films or the strongly disordered nature of the Cu environment, or both, that decreases the apparent coordination number of Cu due to the presence of the surface or grain boundaries or enhanced bond length disorder. Reduction in the long-range order that accompanies both of these effects (the presence of nanosized grains and/or the amorphous nature of the films) is also consistent with the XRD results. The fact that the Sn−Cu coordination number is consistent with the bulk value of 12 indicates that the Sn location within the film is predominantly in the inner volumes or in the subsurface regions of the grains. While it is difficult to evaluate the tendency for cluster formation for such a small concentration of Sn in the CuSn-DAT samples, the absence of Sn−Sn contributions is consistent with the absence of Sn-rich regions. Finally, in CuSn-DAT, the distance of the Cu−Sn bond of ca. 2.65 Å is longer than the Cu−Cu distance (2.54 Å) in bulk Cu but shorter than the Sn−Sn distance (3.04 Å) in bulk Sn. This behavior, typical for alloys,[13,63,64] represents an independent confirmation that Sn substitutes for Cu in the Cu lattice rather than forming a separate metal structure. EXAFS of CuAg-DAT was reported previously and showed a well-mixed alloy.[13]

3.2. Electroreduction of CO_2 in a Flow Reactor. To evaluate the catalytic performance for CO_2 electroreduction, all the Cu-based catalysts electrodeposited on the GDL were characterized in a flow reactor.[15,16] Faradaic efficiencies for all the products on different catalysts are listed in Table S2. Figure 3a shows the current density for CO_2 electroreduction as a

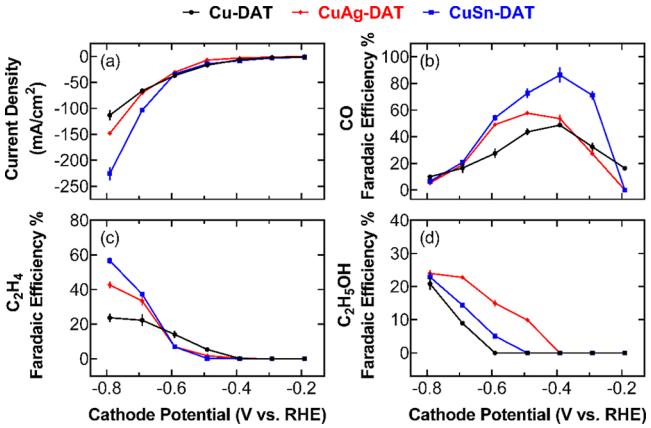

Figure 3. (a) Total current density and Faradaic efficiency for (b) CO production, (c) C_2H_4 production, and (d) C_2H_5OH production for electroreduction of CO_2 as a function of cathode potential on the Cu-DAT (black), CuAg-DAT (red), and CuSn-DAT (blue) electrodes.

function of cathode potential for three different electrodes: Cu-DAT, CuAg-DAT, and CuSn-DAT. At a cathode potential more positive than −0.6 V, all three samples exhibit similar CO_2 electroreduction current densities. At more negative cathode potentials, CuSn-DAT has the highest CO_2 electroreduction current density while Cu-DAT has the lowest. Specifically, the current density values at the cathode potential of −0.8 V on CuSn-DAT, CuAg-DAT, and Cu-DAT are ∼−225, −150, and −110 mA/cm^2, respectively. Interestingly, CuSn-DAT exhibits an ∼20% higher CO_2 electroreduction current density than that of the CuSn-control (Table S2), corresponding to the difference in their electroactive surface area (Table S1).

Figure 3b−d shows the FE of major products (CO, C_2H_4, and C_2H_5OH) as a function of cathode potential. Figure 3b shows that CO production starts at around −0.2 V and increases at more negative potentials to reach a maximum FE value of ∼85% on CuSn-DAT, ∼60% on CuAg-DAT, and ∼50% on Cu-DAT at a cathode potential of −0.4 V. At

DOI: 10.1021/acscatal.9b04368
ACS Catal. 2020, 10, 672−682

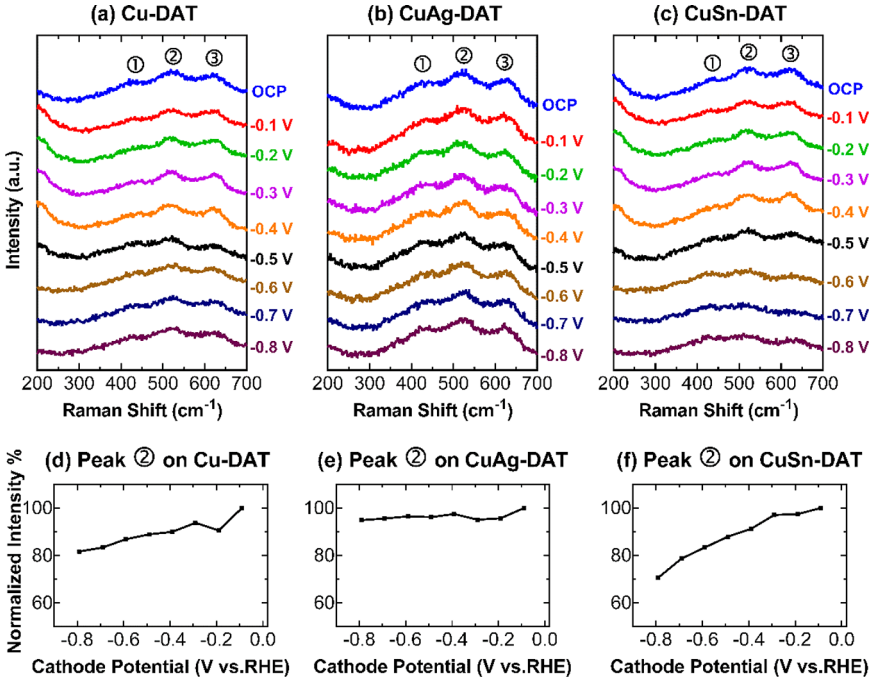

Figure 4. Potential-dependent *in situ* SERS spectra obtained from (a) Cu-DAT, (b) CuAg-DAT, and (c) CuSn-DAT in a flow Raman cell with a 1 M KOH flow rate of 1 mL min^{-1} and an Ar flow rate of 7 SCCM (No CO_2). Normalized intensity of the peak ② as a function of cathode potential on (d) Cu-DAT, (e) CuAg-DAT, and (f) CuSn-DAT.

increasing negative potentials, the FE for CO production decreases while the FEs for both C_2H_4 and C_2H_5OH production increase on all three samples (Figure 3c,d). This trend is consistent with the assumption that the adsorbed CO is an important intermediate of the formation of C_2 products, as has been suggested previously.[15,65−68]

As shown in Figure 3c,d, these three catalysts behave differently relative to the formation of C_2 products in the alkaline flow electrolyzer. CuSn-DAT has the best selectivity toward C_2 products, with the FE for C_2H_4 and C_2H_5OH production reaching nearly 60% and 25%, respectively, at a cathode potential of −0.8 V. In contrast, the maximum FE of C_2 products on Cu-DAT is slightly over 40% at −0.8 V (~20% for ethylene and ~20% for ethanol). CuAg-DAT behaves better than Cu-DAT but still not comparable to CuSn-DAT, with the FE for C_2H_4 and C_2H_5OH production on CuAg-DAT reaching around 40% and 25%, respectively, at a cathode potential of −0.8 V.

3.3. *In Situ* Surface Enhanced Raman Spectroscopy (SERS). *In situ* SERS is performed to understand the different catalytic behaviors attendant the three Cu-based systems. Figure 4a−c reports potential-dependent *in situ* SERS spectra obtained from Cu-DAT, CuAg-DAT, and CuSn-DAT samples in the flow cell with a 1 M KOH (saturated $Ca(OH)_2$ added) flow rate of 1 mL min^{-1} in front of the cathode GDL and an Ar flow rate of 7 SCCM in the back of the cathode. At open circuit potential (OCP), all three Cu-based samples exhibit peaks at 415 cm^{-1} (peak ①), 534 cm^{-1} (peak ②), and 620 cm^{-1} (peak ③). These three peaks are associated with the presence of Cu_2O.[59,69−73] Cu_2O belongs to the O_h point group and exhibits a cubic crystal structure with two formula units per unit cell (Figure S5a). Peak ② at 534 cm^{-1} is the T_{2g} vibrational mode (Figure S5b) from Cu_2O, which is Raman active.[59,69−73] Peak ③ at 620 cm^{-1} is the T_{1u} mode (Figure S5c), which is IR active for a perfect Cu_2O crystal.[59,69−71] However, this Raman silent mode may be activated by the defects within the crystal lattice (including oxygen and copper site defects).[73] The mode at 415 cm^{-1} (peak ①) results from a multiphonon process, which can also be observed via Raman spectroscopy.[59,71,72]

As the potential is made more negative, Figure 4a−c shows that three Cu-based samples exhibit reduced intensity associated with Cu_2O bands compared to the spectrum obtained at OCP. Figure 4d−f reports the potential dependence of the normalized intensity of peak ② on the Cu-DAT, CuAg-DAT, and CuSn-DAT surfaces, respectively. On Cu-DAT, Figure 4d shows that the intensity of peak ② decreases gradually as the potential becomes more negative. At −0.8 V, the intensity of peak ② on the Cu-DAT surface decreases to 80% of the original intensity at OCP. Figure 4e shows that the intensities of Cu_2O related peaks ①−③ remain high at all potentials for CuAg-DAT. The Cu_2O layer on CuAg-DAT is stable at all negative potentials. Figure 4f shows that spectra obtained from CuSn-DAT exhibit decreased intensity associated with peak ② as the potential becomes more negative. At −0.8 V, the intensity of peak ② on the CuSn-DAT surface decreases to 70% of the original intensity at OCP. These spectra show that the Cu_2O is relatively stable without CO_2 introduction even at the negative potentials utilized for CO_2 reduction.

The persistence of oxide-related Raman signals at −0.8 V vs RHE in the flow cell is interesting. The Pourbaix diagram suggests that bulk oxide reduction occurs at −0.36 V vs SHE at pH 14 (0.47 V vs RHE), which is relevant to this measurement.[74] More recently, however, new calculations suggest the presence of Cu oxides and hydroxides at more negative potentials in alkaline conditions.[75] Density functional theory (DFT) calculations suggest that the Cu-terminated Cu_2O (111) surface is favored over the O-terminated surface under conditions relevant to CO_2 reduction and that the

DOI: 10.1021/acscatal.9b04368
ACS Catal. 2020, 10, 672−682

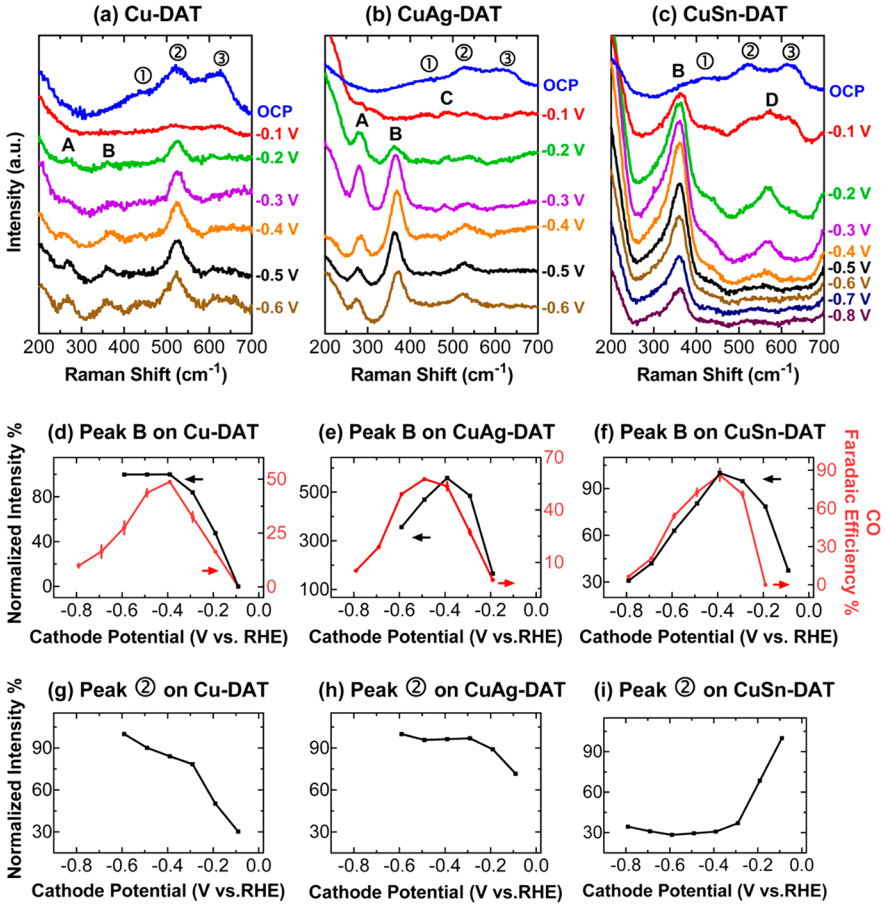

Figure 5. Potential-dependent *in situ* SERS spectra obtained from (a) Cu-DAT, (b) CuAg-DAT, and (c) CuSn-DAT in a flow Raman cell with a 1 M KOH flow rate of 1 mL min^{-1} and a CO_2 flow rate of 7 SCCM. Potential dependence of normalized intensity of the peak B and peak ② on (d, g) Cu-DAT, (e, h) CuAg-DAT, and (f, i) CuSn-DAT.

alkaline environment can stabilize the oxide surface.[76] Many papers discuss copper oxide formation in alkaline conditions. There is less *in situ* work describing the reduction of the oxide at negative potentials. Prior work showed the presence of a thin Cu-oxide related layer at potentials more negative than the region of stability suggested by the Pourbaix diagram. *In situ* vibrational spectra reported by Anderson and co-workers showed the presence of Cu_2O at −0.801 V vs SCE in a 0.1 M NaOH solution (0.213 V vs RHE).[77] Weaver and co-workers also reported the appearance of Cu_2O related bands in the SERS spectra obtained at a potential of −0.95 V vs SCE at pH 13 (0.064 V vs RHE).[78] The difference between the experimental observation of oxide and the Pourbaix diagram was explained by invoking kinetic limitations on the oxide removal process. Calculations suggest that Cu_2O might be stabilized by the presence of a surface hydroxide layer.[79] Interestingly, the presence of such a layer was inferred from *in situ* AFM force curve measurements at potentials negative of the Cu_2O bulk reduction wave in the voltammetry.[80]

Potential-dependent *in situ* SERS during CO_2 reduction was performed on all three Cu-based samples in order to correlate activity with surface speciation. Figure 5 reports the potential-dependent SERS spectra obtained from Cu-DAT, CuAg-DAT, and CuSn-DAT samples in the flow cell with a 1 M KOH flow rate of 1 mL min^{-1} in front of the cathode GDL and a CO_2 flow rate of 7 SCCM in the back of the cathode. The spectrum obtained from Cu-DAT (Figure 5a) exhibits several new peaks appearing when the cathode potential is more negative than −0.2 V. In particular, there are new peaks at 279 cm^{-1} (peak A) and 360 cm^{-1} (peak B). These two peaks are associated with the frustrated ρ(Cu−C−O) rotational mode and the ν(Cu−CO) stretching mode, respectively.[54,81−83] The corresponding normal modes for these two vibrations are shown in Figure S6a,b. The intensities of both peaks A and B are found to increase as the potential is made more negative. Figure 5d shows the normalized intensity of ν(Cu−CO) (peak B) as a function of cathode potential. Interestingly, the intensity of peak B increases and remains high once a cathode potential of −0.4 V is reached. In contrast, the FE for CO production on the Cu-DAT catalyst increases first and decreases at potentials more negative than −0.4 V.

Figure 5a also shows the potential dependence of the Cu_2O related peaks for Cu-DAT. At OCP, the SERS spectrum exhibits all three Cu_2O related peaks ①−③, which is similar to that obtained at OCP without the presence of CO_2 (Figure 4a). At −0.1 V, the SERS spectrum obtained from Cu-DAT with CO_2 exhibits reduced intensity in the Cu_2O-associated bands compared to the spectrum obtained at OCP. In contrast to the SERS measurements obtained without CO_2 where the intensity of the Cu_2O bands decreases gradually as the potential is made more negative (Figure 4d), the intensity of peak ② obtained during CO_2 reduction is found to increase as the potential becomes more negative (Figure 5g). At even more negative potentials, peak ② becomes dominant relative to peaks ① and ③. Interestingly, when peak ② starts to grow at −0.2 V, the Cu−CO related peaks A and B also appear.

DOI: 10.1021/acscatal.9b04368
ACS Catal. 2020, 10, 672−682

Therefore, the presence of Cu−CO on the electrode is correlated with the growth of a Cu_2O layer on the Cu-DAT sample surface.

The frequency of the ν(Cu−CO) stretching mode (peak B) is found to blue-shift by 15 cm^{-1} from the reported ν(Cu−CO) mode on Cu(100),[83] indicating stronger Cu−CO bonding on the Cu-DAT surface relative to Cu(100) in UHV. The increased bond strength has been reported previously from the interaction between the CO molecules and the unsaturated Cu^+ sites on the Cu_2O(100) surface.[84] Prior work also reported the presence of the ν(Cu−CO) stretching mode at 350−360 cm^{-1} on the Cu electrode in aqueous media.[53,54]

The spectrum obtained from CuAg-DAT in the presence of CO_2 (Figure 5b) also exhibits the two Cu−CO related peaks A at 279 cm^{-1} and B at 360 cm^{-1} at negative cathode potentials. Peak A appears at a more positive potential on the CuAg-DAT surface (−0.1 V) relative to Cu-DAT (−0.2 V). While peaks A and B exhibit similar potential dependence at all potentials on Cu-DAT, peak B on the CuAg-DAT surface appears at more negative potentials (−0.2 V) but becomes dominant at potentials more negative than −0.3 V. The intensities of both peaks A and B are found to increase and then decrease as the potential is made more negative. Interestingly, Figure 5e shows that the potential dependence of the normalized intensity of ν(Cu−CO) (peak B) is similar to the potential dependence of the FE for CO production on the CuAg-DAT catalyst. Peak C at 480 cm^{-1} is another new peak seen on the CuAg-DAT surface but not present on Cu-DAT. Peak C is associated with the presence of $Cu(OH)_2$.[77,78,85,86]

Figure 5h reports the potential dependence of the normalized intensity of peak ② on the CuAg-DAT surface during CO_2 reduction. The intensity of peak ② increases and remains high once a cathode potential of −0.3 V is reached. During CO_2 reduction, only the T_{2g} vibrational mode (peak ②) remains on the surface. In contrast, the SERS spectra obtained in the absence of CO_2 exhibited relatively constant intensity for peak ② at all negative potentials on the CuAg-DAT surface (Figure 4b,e; Table 2).

Table 2. Assignments of Raman Peaks and Corresponding Vibrational Modes

peaks	Raman shift (cm^{-1})	species	assignments	reference
①	415	Cu_2O	multiphonon	59, 71, 72
②	535	Cu_2O	T_{2g}	59, 69−73
③	620	Cu_2O	T_{1u}	59, 69−71
A	279	CO	frustrated ρ(Cu−C−O)	54, 81−83
B	360	CO	ν(Cu−CO)	54, 81−83
C	480	$Cu(OH)_2$	Cu−O−H deformation	77, 78, 85, 86
D	570	SnO_2	A_{1g}	87−90

Figure 5c reports the potential-dependent SERS spectrum obtained from CuSn-DAT in the presence of CO_2. In contrast to the Cu-DAT and CuAg-DAT cases, only one Cu−CO related peak, peak B at 360 cm^{-1}, is observed from CuSn-DAT at negative potentials. The energy of peak B on CuSn-DAT is the same as that found on Cu-DAT, suggesting that putative interactions between CO and surface Sn are not large. The absence of peak A may be related to the increased CO concentration on the CuSn-DAT surface. Indeed, prior work in the ultra high vacuum (UHV) environment showed that, as the surface CO concentration was increased, the intensity of peak B on the Cu also increased at the expense of peak A.[81,91] As shown in Figure 5f, the potential dependence of the normalized intensity of ν(Cu−CO) (peak B) mirrors the potential dependence of the FE for CO production from the CuSn-DAT sample. Figure 5c also shows the presence of a new peak on the CuSn-DAT surface at 570 cm^{-1}. This new peak D is associated with the A_{1g} Sn−O stretch and is typically observed in Raman spectra obtained from SnO_2 nanocrystals.[87−90]

Figure 5i shows the potential dependence of Cu_2O for CuSn-DAT during CO_2 reduction. As the potential is made more negative, the intensity of peak ② decreases dramatically. At a cathode potential more negative than −0.3 V, the intensity of peak ② decreases to ∼30% of its intensity at OCP. However, under Ar, CuSn-DAT exhibits evidence for the presence of Cu_2O at all negative potentials, with somewhat decreasing intensity at negative potentials. Therefore, the disappearance of the Cu_2O layer on the electrode is correlated with the reduction of CO_2 for the CuSn-DAT sample.

The relative ratio of bicarbonate to carbonate peaks in the SERS provides a measure of the surface pH.[92] In the case of CuSn-DAT, SERS (Figure S7c) shows the presence of only a carbonate peak (peak F), suggesting that the surface pH is >11. Alternatively, SERS from Cu-DAT and CuAg-DAT (Figure S7a,b) shows the presence of both carbonate (peak F) and bicarbonate (peak E) signals, suggesting the surface pH is lower.

The *in situ* SERS spectra obtained from all three Cu-alloy samples suggest that Cu_2O on the surface plays a significant role in the reduction of CO_2 to CO. To further investigate the correlation between Cu_2O and CO production, Figure 6a−c shows the intensity ratio of peaks B/② (ν(Cu−CO)/T_{2g}(Cu_2O)) on Cu-DAT, CuAg-DAT, and CuSn-DAT as a function of cathode potential. On all three Cu-alloy samples, the intensity ratio of peak B/② increases first and decreases as the potential is made more negative. Interestingly, the potential dependence of the intensity ratio of peak B/② is similar to the potential dependence of the FE for CO production on all three Cu-alloy samples. At −0.4 V, the intensity ratio of peak B/② is the largest on CuSn-DAT (∼2000) compared to that on Cu-DAT (∼45) and CuAg-DAT (∼500). The large value of the intensity ratio of peak B/② for CuSn-DAT corresponds to the highest FE for CO production obtained from this sample. The intermediate value obtained for CuAg-DAT corresponds to the intermediate FE for CO production. The lower value obtained for Cu-DAT likewise corresponds to the lower FE for CO production obtained from this sample. Thus, the reduction of CO_2 to CO is related to both the Cu−CO adsorption and the presence of a Cu_2O layer on the Cu surface.

4. DISCUSSION

Figure 6a−c shows that the maintenance of a more substantial Cu_2O layer on the Cu surface during CO_2 reduction leads to a lower FE for CO production. We next address the origin of the Cu_2O layer in the presence of CO_2. Calculations suggest that oxygen atom transfer from CO_2 to make OH^- or H_2O is a step during CO_2 reduction to make CO (Scheme 1).[31,65,67] This suggests that surface alkalinity and therefore the amount of Cu_2O should increase during the course of CO_2 reduction. Indeed, this increase in Cu_2O is seen during CO_2 reduction on Cu-DAT and to a lesser extent on CuAg-DAT with more

DOI: 10.1021/acscatal.9b04368
ACS Catal. 2020, 10, 672−682

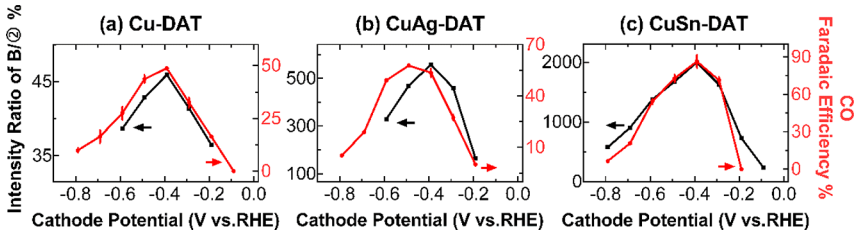

Figure 6. Intensity ratio of peak (B/②) and the FE for CO production as a function of cathode potential on (a) Cu-DAT, (b) CuAg-DAT, and (c) CuSn-DAT.

Scheme 1. Proposed Mechanism of Reduction of CO_2 to CO on (a) Cu-DAT and (b) CuSn-DAT Surfaces in Alkaline Solutions Showing the Disposition of Surface Oxides

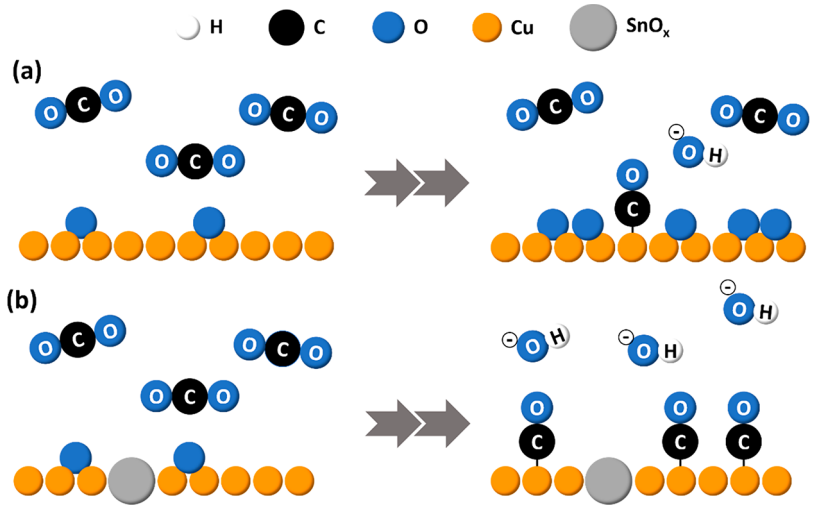

negative potentials. As the amount of Cu_2O increases on the electrode surface, the FE for CO production achieves a maximum and then decreases. This correlation suggests that Cu_2O is a byproduct of CO_2 reduction but also blocks active sites at higher concentrations on the surface. Indeed, calculations suggest that, while thin layers of Cu_2O are beneficial for CO_2 reduction, thick layers are not.[51]

In the presence of alloyed Ag or Sn, the FE for CO production increases. Correspondingly, the relative amount of CO vs Cu_2O on the surface increases. The origin of this increase likely relates to the ability of the alloyed element to remove oxygen from the Cu surface (or equivalently to reduce the Cu surface), yielding increased density of the active sites. Interestingly, the SERS from CuSn-DAT shows the presence of only a carbonate peak, indicating the surface is relatively basic even though there is less Cu_2O compared with the Cu-DAT or CuAg-DAT cases. This result suggests that Cu_2O is being removed from the Cu surface through the agency of the alloyed Sn. Indeed, SERS spectra show the presence of SnO_2 at intermediate potentials. The ability to reduce Cu_2O leads to higher FE for CO production. CuAg-DAT exhibits intermediate results for CO production due to the reduced oxophilicity of the Ag compared with Sn.[93]

Finally, we address the origin of increased FE for C_2 products also seen with the alloy surfaces compared to Cu-DAT. The presence of alloying leads to the increased density of CO on the electrode surface. Indeed, the absence of peak A in the CuSn-DAT sample indicates the presence of a dense CO layer on the CuSn-DAT surface. The increased density of CO is associated with increased FE for C_2 products. The mechanism proposed by Koper and co-workers suggests that the rate determining step (RDS) of ethylene formation would be the dimerization of CO.[94] In addition, higher local pH on the CuSn-DAT surface relative to Cu-DAT and CuAg-DAT can also contribute to a higher FE for C_2 products. CO dimerization and ethylene formation are reported to be enhanced on a high local pH electrode.[94,95] The lower FE for C_2 products on Cu-DAT may also be a consequence of the thick oxide layer on the electrode surface. The stronger binding of the CO* intermediate to the Cu_2O relative to metallic Cu leads to a less reactive CO and consequent lower efficacy for the hydrogenation process.[48,51] We note that the CuSn-DAT sample is most efficient at ethylene formation at very negative potentials where the amount of oxide on the surface, as interrogated by SERS, is low relative to more positive potentials. This observation suggests that Cu_2O by itself is not necessary for C_2 product formation. Rather, a high concentration of surface CO leads to enhanced C_2 production.

In summary, the removal of Cu_2O from the Cu surface through the agency of the alloyed Sn may result in more active Cu sites for the CO adsorption. With increased density of CO on the electrode surface, C−C coupling could be facilitated to form more C_2 products. Thus, CuSn-DAT has an enhanced FE for CO and C_2H_4 production compared to Cu-DAT and CuAg-DAT.

5. CONCLUSION

In this study, we compare the CO_2 reduction performance of three electrodes based on Cu alone, a Cu/Ag alloy, and a Cu/Sn alloy. The electrode films were deposited onto a GDL by using DAT as a deposition bath inhibitor and exhibited high

DOI: 10.1021/acscatal.9b04368
ACS Catal. 2020, 10, 672−682

surface area and porous structure. CO_2 reduction in a flow reactor shows that the three Cu-based electrodes all exhibit high activity and selectivity for the production of CO and C_2 products. CuSn-DAT exhibits the highest activity, followed by CuAg-DAT.

Potential-dependent *in situ* SERS spectra obtained in a flow cell from the three samples show the presence of an inverse correlation between the magnitude of the Cu_2O layer and CO and C_2 production from the sample. While Cu-DAT exhibits an increasing Cu_2O presence during the course of CO_2 reduction, CuSn-DAT exhibits decreasing Cu_2O intensity in the potential-dependent SERS. This decrease in Cu_2O intensity is correlated with relatively more Cu−CO intensity. The data suggest that the presence of Sn in the sample helps to remove oxide from Cu centers, leading to higher CO availability on the electrode surface during CO_2 reduction. This higher availability is correlated with increased efficiency for CO and C_2 product formation.

■ ASSOCIATED CONTENT

Supporting Information

The Supporting Information is available free of charge at https://pubs.acs.org/doi/10.1021/acscatal.9b04368.

Characterization (electroactive surface area, XRD, XPS, and XAFS), Faradaic efficiencies for all products, and *in situ* Raman flow cell setup and spectra (PDF)

■ AUTHOR INFORMATION

Corresponding Author

*E-mail: agewirth@illinois.edu.

ORCID

Xinyi Chen: 0000-0002-6990-5233
Danielle A. Henckel: 0000-0003-2640-7127
Anatoly I. Frenkel: 0000-0002-5451-1207
Tim T. Fister: 0000-0001-6537-6170
Paul J. A. Kenis: 0000-0001-7348-0381
Andrew A. Gewirth: 0000-0003-4400-9907

Notes

The authors declare no competing financial interest.

■ ACKNOWLEDGMENTS

The authors gratefully acknowledge the support of the International Institute for Carbon Neutral Energy Research (WPI-I2CNER), sponsored by the Japanese Ministry of Education, Culture, Sports, Science and Technology. D.A.H. gratefully acknowledges Shell's New Energy Research and Technology (NERT) program for providing funding. A.I.F. acknowledges support of the U.S. DOE Grant No. DE-FG02-03ER15476. We thank Dr. Richard T. Haasch for performing XPS and the SCS machine shop (in particular Michael A. Harland) for their help in designing the *in situ* flow cell for the SERS measurements. We also thank the SCS NMR lab (Dr. Dean Olsen and Dr. Lingyang Zhu) for their help in NMR measurements.

■ REFERENCES

(1) International Energy Agency *CO_2 Emissions from Fuel Combustion 2017*; Organization for Economic Cooperation and Development, 2017.

(2) The Keeling Curve; 2019; https://scripps.ucsd.edu/programs/keelingcurve/.

(3) Ussiri, D. A. N.; Lal, R. *Carbon Sequestration for Climate Change Mitigation and Adaptation*, 1st ed.; Springer International Publishing: Cham, Switzerland, 2017; p 549.

(4) Federsel, C.; Jackstell, R.; Beller, M. State-of-the-Art Catalysts for Hydrogenation of Carbon Dioxide. *Angew. Chem., Int. Ed.* **2010**, *49*, 6254−6257.

(5) Hansen, J.; Kharecha, P.; Sato, M.; Masson-Delmotte, V.; Ackerman, F.; Beerling, D. J.; Hearty, P. J.; Hoegh-Guldberg, O.; Hsu, S. L.; Parmesan, C.; Rockstrom, J.; Rohling, E. J.; Sachs, J.; Smith, P.; Steffen, K.; Van Susteren, L.; von Schuckmann, K.; Zachos, J. C. Assessing "Dangerous Climate Change": Required Reduction of Carbon Emissions to Protect Young People, Future Generations and Nature. *PLoS One* **2013**, *8*, No. e81648.

(6) Lenzen, M. Current State of Development of Electricity-Generating Technologies: A Literature Review. *Energies* **2010**, *3*, 462−591.

(7) Willrich, M. Electricity Transmission Policy for America: Enabling a Smart Grid, End-to-End. *Electr. J.* **2009**, *22*, 77−82.

(8) Qiao, J.; Liu, Y.; Hong, F.; Zhang, J. A Review of Catalysts for the Electroreduction of Carbon Dioxide to Produce Low-Carbon Fuels. *Chem. Soc. Rev.* **2014**, *43*, 631−75.

(9) Gattrell, M.; Gupta, N.; Co, A. A Review of the Aqueous Electrochemical Reduction of CO_2 to Hydrocarbons at Copper. *J. Electroanal. Chem.* **2006**, *594*, 1−19.

(10) Hori, Y. Electrochemical CO_2 Reduction on Metal Electrodes. In *Modern Aspects of Electrochemistry*; Vayenas, C. G., White, R. E., Gamboa-Aldeco, M. E., Eds.; Springer New York: New York, NY, 2008; pp 89−189.

(11) Lim, R. J.; Xie, M.; Sk, M. A.; Lee, J.-M.; Fisher, A.; Wang, X.; Lim, K. H. A Review on the Electrochemical Reduction of CO_2 in Fuel Cells, Metal Electrodes and Molecular Catalysts. *Catal. Today* **2014**, *233*, 169−180.

(12) Hoang, T. T. H.; Ma, S.; Gold, J. I.; Kenis, P. J. A.; Gewirth, A. A. Nanoporous Copper Films by Additive-Controlled Electrodeposition: CO_2 Reduction Catalysis. *ACS Catal.* **2017**, *7*, 3313−3321.

(13) Hoang, T. T. H.; Verma, S.; Ma, S.; Fister, T. T.; Timoshenko, J.; Frenkel, A. I.; Kenis, P. J. A.; Gewirth, A. A. Nanoporous Copper-Silver Alloys by Additive-Controlled Electrodeposition for the Selective Electroreduction of CO_2 to Ethylene and Ethanol. *J. Am. Chem. Soc.* **2018**, *140*, 5791−5797.

(14) Ma, S.; Sadakiyo, M.; Heima, M.; Luo, R.; Haasch, R. T.; Gold, J. I.; Yamauchi, M.; Kenis, P. J. Electroreduction of Carbon Dioxide to Hydrocarbons Using Bimetallic Cu-Pd Catalysts with Different Mixing Patterns. *J. Am. Chem. Soc.* **2017**, *139*, 47−50.

(15) Ma, S.; Sadakiyo, M.; Luo, R.; Heima, M.; Yamauchi, M.; Kenis, P. J. A. One-Step Electrosynthesis of Ethylene and Ethanol from CO_2 in an Alkaline Electrolyzer. *J. Power Sources* **2016**, *301*, 219−228.

(16) Verma, S.; Lu, X.; Ma, S.; Masel, R. I.; Kenis, P. J. The effect of electrolyte composition on the electroreduction of CO_2 to CO on Ag based gas diffusion electrodes. *Phys. Chem. Chem. Phys.* **2016**, *18*, 7075−7084.

(17) Zhu, W.; Michalsky, R.; Metin, O.; Lv, H.; Guo, S.; Wright, C. J.; Sun, X.; Peterson, A. A.; Sun, S. Monodisperse Au Nanoparticles for Selective Electrocatalytic Reduction of CO2 to CO. *J. Am. Chem. Soc.* **2013**, *135*, 16833−16836.

(18) Liang, C.; Kim, B.; Yang, S.; Yang Liu, Y. L.; Francisco Woellner, C.; Li, Z.; Vajtai, R.; Yang, W.; Wu, J.; Kenis, P. J. A.; Ajayan, Pulickel M. High Efficiency Electrochemical Reduction of CO_2 Beyond the Two-Electron Transfer Pathway on Grain Boundary Rich Ultra-Small SnO_2 Nanoparticles. *J. Mater. Chem. A* **2018**, *6*, 10313−10319.

(19) Verma, S.; Hamasaki, Y.; Kim, C.; Huang, W.; Lu, S.; Jhong, H.-R. M.; Gewirth, A. A.; Fujigaya, T.; Nakashima, N.; Kenis, P. J. A. Insights into the Low Overpotential Electroreduction of CO_2 to CO on a Supported Gold Catalyst in an Alkaline Flow Electrolyzer. *ACS Energy Lett.* **2018**, *3*, 193−198.

DOI: 10.1021/acscatal.9b04368
ACS Catal. 2020, 10, 672−682

(20) Weng, Z.; Jiang, J.; Wu, Y.; Wu, Z.; Guo, X.; Materna, K. L.; Liu, W.; Batista, V. S.; Brudvig, G. W.; Wang, H. Electrochemical CO_2 Reduction to Hydrocarbons on a Heterogeneous Molecular Cu Catalyst in Aqueous Solution. *J. Am. Chem. Soc.* **2016**, *138*, 8076−8079.
(21) Wang, H.; Luo, H.; Fallgren, P. H.; Jin, S.; Ren, Z. J. Bioelectrochemical system platform for sustainable environmental remediation and energy generation. *Biotechnol. Adv.* **2015**, *33*, 317−34.
(22) Jez, J. M.; Lee, S. G.; Sherp, A. M. The Next Green Movement: Plant Biology for the Environment and Sustainability. *Science* **2016**, *353*, 1241−1244.
(23) Zhang, S.; Kang, P.; Meyer, T. J. Nanostructured Tin Catalysts for Selective Electrochemical Reduction of Carbon Dioxide to Formate. *J. Am. Chem. Soc.* **2014**, *136*, 1734−1737.
(24) Zheng, X.; De Luna, P.; García de Arquer, F. P.; Zhang, B.; Becknell, N.; Ross, M. B.; Li, Y.; Banis, M. N.; Li, Y.; Liu, M.; Voznyy, O.; Dinh, C. T.; Zhuang, T.; Stadler, P.; Cui, Y.; Du, X.; Yang, P.; Sargent, E. H. Sulfur-Modulated Tin Sites Enable Highly Selective Electrochemical Reduction of CO_2 to Formate. *Joule* **2017**, *1*, 794−805.
(25) Li, F.; Chen, L.; Knowles, G. P.; MacFarlane, D. R.; Zhang, J. Hierarchical Mesoporous SnO_2 Nanosheets on Carbon Cloth: A Robust and Flexible Electrocatalyst for CO_2 Reduction with High Efficiency and Selectivity. *Angew. Chem., Int. Ed.* **2017**, *56*, 505−509.
(26) Wang, Q.; Wang, X.; Wu, C.; Cheng, Y.; Sun, Q.; Dong, H.; Yu, H. Electrodeposition of Tin on Nafion-Bonded Carbon Black as an Active Catalyst Layer for Efficient Electroreduction of CO_2 to Formic Acid. *Sci. Rep.* **2017**, *7*, 13711.
(27) Lee, C. H.; Kanan, M. W. Controlling H^+ vs CO_2 Reduction Selectivity on Pb Electrodes. *ACS Catal.* **2015**, *5*, 465−469.
(28) Gao, S.; Lin, Y.; Jiao, X.; Sun, Y.; Luo, Q.; Zhang, W.; Li, D.; Yang, J.; Xie, Y. Partially Oxidized Atomic Cobalt Layers for Carbon Dioxide Electroreduction to Liquid Fuel. *Nature* **2016**, *529*, 68−71.
(29) Hori, Y.; Kikuchi, K.; Murata, A.; Suzuki, S. Production of Methane and Ethylene in Electrochemical Reduction of Carbon Dioxide at Copper Electrode in Aqueous Hydrogencarbonate Solution. *Chem. Lett.* **1986**, *15*, 897−898.
(30) Hori, Y.; Murata, A.; Tsukamoto, T.; Wakebe, H.; Koga, O.; Yamazaki, H. Adsorption of Carbon Monoxide at a Copper Electrode Accompanied by Electron Transfer Observed by Voltammetry and IR Spectroscopy. *Electrochim. Acta* **1994**, *39*, 2495−2500.
(31) Hori, Y.; Wakebe, H.; Tsukamoto, T.; Koga, O. Electrocatalytic Process of CO Selectivity in Electrochemical Reduction of CO_2 at Metal Electrodes in Aqueous Media. *Electrochim. Acta* **1994**, *39*, 1833−1839.
(32) Kim, D.; Resasco, J.; Yu, Y.; Asiri, A. M.; Yang, P. Synergistic Geometric and Electronic Effects for Electrochemical Reduction of Carbon Dioxide Using Gold-Copper Bimetallic Nanoparticles. *Nat. Commun.* **2014**, *5*, 4948.
(33) Li, Y. C.; Wang, Z.; Yuan, T.; Nam, D. H.; Luo, M.; Wicks, J.; Chen, B.; Li, J.; Li, F.; de Arquer, F. P. G.; Wang, Y.; Dinh, C. T.; Voznyy, O.; Sinton, D.; Sargent, E. H. Binding Site Diversity Promotes CO_2 Electroreduction to Ethanol. *J. Am. Chem. Soc.* **2019**, *141*, 8584−8591.
(34) Li, Q.; Fu, J.; Zhu, W.; Chen, Z.; Shen, B.; Wu, L.; Xi, Z.; Wang, T.; Lu, G.; Zhu, J. J.; Sun, S. Tuning Sn-Catalysis for Electrochemical Reduction of CO_2 to CO via the Core/Shell Cu/SnO_2 Structure. *J. Am. Chem. Soc.* **2017**, *139*, 4290−4293.
(35) Zeng, J.; Bejtka, K.; Ju, W.; Castellino, M.; Chiodoni, A.; Sacco, A.; Farkhondehfal, M. A.; Hernández, S.; Rentsch, D.; Battaglia, C.; Pirri, C. F. Advanced Cu-Sn Foam for Selectively Converting CO_2 to CO in Aqueous Solution. *Appl. Catal., B* **2018**, *236*, 475−482.
(36) Sarfraz, S.; Garcia-Esparza, A. T.; Jedidi, A.; Cavallo, L.; Takanabe, K. Cu-Sn Bimetallic Catalyst for Selective Aqueous Electroreduction of CO_2 to CO. *ACS Catal.* **2016**, *6*, 2842−2851.
(37) Katah, A.; Uchida, H.; Shibata, M.; Watanabe, M. Design of Electrocatalyst for CO_2 Reduction V. Effect of the Microcrystalline Structures of Cu-Sn and Cu-Zn Alloys on the Electrocatalysis of CO_2 Reduction. *J. Electrochem. Soc.* **1994**, *141*, 2054−2058.
(38) Huo, S.; Weng, Z.; Wu, Z.; Zhong, Y.; Wu, Y.; Fang, J.; Wang, H. Coupled Metal/Oxide Catalysts with Tunable Product Selectivity for Electrocatalytic CO_2 Reduction. *ACS Appl. Mater. Interfaces* **2017**, *9*, 28519−28526.
(39) He, J.; Dettelbach, K. E.; Huang, A.; Berlinguette, C. P. Brass and Bronze as Effective CO_2 Reduction Electrocatalysts. *Angew. Chem., Int. Ed.* **2017**, *56*, 16579−16582.
(40) Camilo, M.; Silva, W.; Lima, F. Investigation of Electrocatalysts for Selective Reduction of CO_2 to CO: Monitoring the Reaction Products by on line Mass Spectrometry and Gas Chromatography. *J. Braz. Chem. Soc.* **2017**, *28*, 1803−1815.
(41) Lv, W.; Zhou, J.; Kong, F.; Fang, H.; Wang, W. Porous Tin-Based Film Deposited on Copper Foil for Electrochemical Reduction of Carbon Dioxide to Formate. *Int. J. Hydrogen Energy* **2016**, *41*, 1585−1591.
(42) Morimoto, M.; Takatsuji, Y.; Yamasaki, R.; Hashimoto, H.; Nakata, I.; Sakakura, T.; Haruyama, T. Electrodeposited Cu-Sn Alloy for Electrochemical CO_2 Reduction to $CO/HCOO^-$. *Electrocatalysis* **2018**, *9*, 323−332.
(43) Qin, B.; Wang, H.; Peng, F.; Yu, H.; Cao, Y. Effect of the Surface Roughness of Copper Substrate on Three-Dimensional Tin Electrode for Electrochemical Reduction of CO_2 into HCOOH. *J. CO2 Util.* **2017**, *21*, 219−223.
(44) Wang, J.; Ji, Y.; Shao, Q.; Yin, R.; Guo, J.; Li, Y.; Huang, X. Phase and structure modulating of bimetallic CuSn nanowires boosts electrocatalytic conversion of CO_2. *Nano Energy* **2019**, *59*, 138−145.
(45) Wang, Y.; Zhou, J.; Lv, W.; Fang, H.; Wang, W. Electrochemical Reduction of CO_2 to Formate Catalyzed by Electroplated Tin Coating on Copper Foam. *Appl. Surf. Sci.* **2016**, *362*, 394−398.
(46) Zhang, X.; Li, F.; Zhang, Y.; Bond, A. M.; Zhang, J. Stannate Derived Bimetallic Nanoparticles for Electrocatalytic CO_2 Reduction. *J. Mater. Chem. A* **2018**, *6*, 7851−7858.
(47) Zhao, C.; Wang, J. Electrochemical Reduction of CO_2 to Formate in Aqueous Solution Using Electro-Deposited Sn Catalysts. *Chem. Eng. J.* **2016**, *293*, 161−170.
(48) Li, C. W.; Kanan, M. W. CO_2 Reduction at Low Overpotential on Cu Electrodes Resulting from the Reduction of Thick Cu_2O Films. *J. Am. Chem. Soc.* **2012**, *134*, 7231−7234.
(49) Mistry, H.; Varela, A. S.; Bonifacio, C. S.; Zegkinoglou, I.; Sinev, I.; Choi, Y. W.; Kisslinger, K.; Stach, E. A.; Yang, J. C.; Strasser, P.; Cuenya, B. R. Highly Selective Plasma-Activated Copper Catalysts for Carbon Dioxide Reduction to Ethylene. *Nat. Commun.* **2016**, *7*, 12123.
(50) Kas, R.; Kortlever, R.; Milbrat, A.; Koper, M. T.; Mul, G.; Baltrusaitis, J. Electrochemical CO_2 Reduction on Cu_2O-Derived Copper Nanoparticles: Controlling the Catalytic Selectivity of Hydrocarbons. *Phys. Chem. Chem. Phys.* **2014**, *16*, 12194−12201.
(51) Chang, X.; Wang, T.; Zhao, Z. J.; Yang, P.; Greeley, J.; Mu, R.; Zhang, G.; Gong, Z.; Luo, Z.; Chen, J.; Cui, Y.; Ozin, G. A.; Gong, J. Tuning Cu/Cu_2O Interfaces for the Reduction of Carbon Dioxide to Methanol in Aqueous Solutions. *Angew. Chem., Int. Ed.* **2018**, *57*, 15415−15419.
(52) Ren, D.; Ang, B. S.-H.; Yeo, B. S. Tuning the Selectivity of Carbon Dioxide Electroreduction toward Ethanol on Oxide-Derived Cu_xZn Catalysts. *ACS Catal.* **2016**, *6*, 8239−8247.
(53) Batista, E. A.; Temperini, M. L. A. Spectroscopic Evidences of the Presence of Hydrogenated Species on the Surface of Copper During CO_2 Electroreduction at Low Cathodic Potentials. *J. Electroanal. Chem.* **2009**, *629*, 158−163.
(54) Gunathunge, C. M.; Li, X.; Li, J.; Hicks, R. P.; Ovalle, V. J.; Waegele, M. M. Spectroscopic Observation of Reversible Surface Reconstruction of Copper Electrodes under CO_2 Reduction. *J. Phys. Chem. C* **2017**, *121*, 12337−12344.
(55) Smith, B. D.; Irish, D. E. A Surface Enhanced Raman Scattering Study of the Intermediate and Poisoning Species Formed during the Electrochemical Reduction of CO_2 on Copper. *J. Electrochem. Soc.* **1997**, *144*, 4288−4296.

DOI: 10.1021/acscatal.9b04368
ACS Catal. 2020, 10, 672−682

(56) Ross, M. B.; Dinh, C. T.; Li, Y.; Kim, D.; De Luna, P.; Sargent, E. H.; Yang, P. Tunable Cu Enrichment Enables Designer Syngas Electrosynthesis from CO_2. *J. Am. Chem. Soc.* **2017**, *139*, 9359−9363.
(57) Oda, I.; Ogasawara, H.; Ito, M. Carbon Monoxide Adsorption on Copper and Silver Electrodes during Carbon Dioxide Electroreduction Studied by Infrared Reflection Absorption Spectroscopy and Surface-Enhanced Raman Spectroscopy. *Langmuir* **1996**, *12*, 1094−1097.
(58) Kwon, Y.; Lum, Y.; Clark, E. L.; Ager, J. W.; Bell, A. T. CO_2 Electroreduction with Enhanced Ethylene and Ethanol Selectivity by Nanostructuring Polycrystalline Copper. *ChemElectroChem* **2016**, *3*, 1012−1019.
(59) Jiang, S.; Klingan, K.; Pasquini, C.; Dau, H. New Aspects of Operando Raman Spectroscopy Applied to Electrochemical CO_2 Reduction on Cu Foams. *J. Chem. Phys.* **2019**, *150*, 041718.
(60) Wu, G. Y.; Bae, S. E.; Gewirth, A. A.; Gray, J.; Zhu, X. D.; Moffat, T. P.; Schwarzacher, W. Pb Electrodeposition on Polycrystalline Cu in the Presence and Absence of Cl^-: A Combined Oblique Incidence Reflectivity Difference and in situ AFM Study. *Surf. Sci.* **2007**, *601*, 1886−1891.
(61) Schultz, Z. D.; Feng, Z. V.; Biggin, M. E.; Gewirth, A. A. Vibrational Spectroscopic and Mass Spectrometric Studies of the Interaction of Bis(3-sulfopropyl)-disulfide with Cu Surfaces. *J. Electrochem. Soc.* **2006**, *153*, C97−C107.
(62) Kim, M. G.; Sim, S.; Cho, J. Novel Core-Shell Sn-Cu Anodes for Lithium Rechargeable Batteries Prepared by a Redox-Transmetalation Reaction. *Adv. Mater.* **2010**, *22*, 5154−8.
(63) Bradley, J. S.; Via, G. H.; Bonneviot, L.; Hill, E. W. Infrared and EXAFS Study of Compositional Effects in Nanoscale Colloidal Palladium-Copper Alloys. *Chem. Mater.* **1996**, *8*, 1895−1903.
(64) Cohen, R. L.; Feldman, L. C.; West, K. W.; Kincaid, B. M. Displacement around a Dissolved Impurity Atom in a Metal: Sn in Cu. *Phys. Rev. Lett.* **1982**, *49*, 1416−1419.
(65) Kortlever, R.; Shen, J.; Schouten, K. J.; Calle-Vallejo, F.; Koper, M. T. Catalysts and Reaction Pathways for the Electrochemical Reduction of Carbon Dioxide. *J. Phys. Chem. Lett.* **2015**, *6*, 4073−4082.
(66) Montoya, J. H.; Shi, C.; Chan, K.; Norskov, J. K. Theoretical Insights into a CO Dimerization Mechanism in CO_2 Electroreduction. *J. Phys. Chem. Lett.* **2015**, *6*, 2032−2037.
(67) Schouten, K. J. P.; Kwon, Y.; van der Ham, C. J. M.; Qin, Z.; Koper, M. T. M. A New Mechanism for the Selectivity to C_1 and C_2 Species in the Electrochemical Reduction of Carbon Dioxide on Copper Electrodes. *Chem. Sci.* **2011**, *2*, 1902−1909.
(68) Kuhl, K. P.; Cave, E. R.; Abram, D. N.; Jaramillo, T. F. New Insights into the Electrochemical Reduction of Carbon Dioxide on Metallic Copper Surfaces. *Energy Environ. Sci.* **2012**, *5*, 7050−7059.
(69) Sander, T.; Reindl, C. T.; Giar, M.; Eifert, B.; Heinemann, M.; Heiliger, C.; Klar, P. J. Correlation of Intrinsic Point Defects and the Raman Modes of Cuprous Oxide. *Phys. Rev. B: Condens. Matter Mater. Phys.* **2014**, *90*, 045203.
(70) Powell, D.; Compaan, A.; Macdonald, J. R.; Forman, R. A. Raman-Scattering Study of Ion-Implantation-Produced Damage in Cu_2O. *Phys. Rev. B* **1975**, *12*, 20−25.
(71) Singhal, A.; Pai, M. R.; Rao, R.; Pillai, K. T.; Lieberwirth, I.; Tyagi, A. K. Copper(I) Oxide Nanocrystals - One Step Synthesis, Characterization, Formation Mechanism, and Photocatalytic Properties. *Eur. J. Inorg. Chem.* **2013**, *2013*, 2640−2651.
(72) Balkanski, M.; Nusimovici, M. A.; Reydellet, J. First Order Raman Spectrum of Cu_2O. *Solid State Commun.* **1969**, *7*, 815−818.
(73) Deng, Y.; Handoko, A. D.; Du, Y.; Xi, S.; Yeo, B. S. In Situ Raman Spectroscopy of Copper and Copper Oxide Surfaces during Electrochemical Oxygen Evolution Reaction: Identification of CuIII Oxides as Catalytically Active Species. *ACS Catal.* **2016**, *6*, 2473−2481.
(74) Pourbaix, M. *Atlas of Electrochemical Equilibria in Aqueous Solutions*, Second English ed.; National Association of Corrosion: Houston, TX, 1974; p 644.
(75) Beverskog, B. P. I. Revised Pourbaix Diagrams for Copper at 25 to 300°C. *J. Electrochem. Soc.* **1997**, *144*, 3476−3483.
(76) Nie, X.; Griffin, G. L.; Janik, M. J.; Asthagiri, A. Surface phases of $Cu_2O(111)$ under CO_2 electrochemical reduction conditions. *Catal. Commun.* **2014**, *52*, 88−91.
(77) Hamilton, J. C.; Farmer, J. C.; Anderson, R. J. In Situ Raman Spectroscopy of Anodic Films Formed on Copper and Silver in Sodium Hydroxide Solution. *J. Electrochem. Soc.* **1986**, *133*, 739−745.
(78) Chan, H. Y. H.; Takoudis, C. G.; Weaver, M. J. Oxide Film Formation and Oxygen Adsorption on Copper in Aqueous Media As Probed by Surface-Enhanced Raman Spectroscopy. *J. Phys. Chem. B* **1999**, *103*, 357−365.
(79) Islam, M. M.; Diawara, B.; Maurice, V.; Marcus, P. First Principles Investigation on the Stabilization Mechanisms of the Polar Copper Terminated $Cu_2O(111)$ Surface. *Surf. Sci.* **2009**, *603*, 2087−2095.
(80) Kang, M.; Gewirth, A. A. Voltammetric and Force Spectroscopic Examination of Oxide Formation on Cu(111) in Basic Solution. *J. Phys. Chem. B* **2002**, *106*, 12211−12220.
(81) Akemann, W.; Otto, A. The effect of atomic scale surface disorder on bonding and activation of adsorbates: vibrational properties of CO and CO_2 on copper. *Surf. Sci.* **1993**, *287*, 104−109.
(82) Akemann, W.; Otto, A. Vibrational Modes of CO Adsorbed on Disordered Copper Films. *J. Raman Spectrosc.* **1991**, *22*, 797−803.
(83) Hirschmugl, C. J.; Williams, G. P.; Hoffmann, F. M.; Chabal, Y. J. Adsorbate-substrate resonant interactions observed for CO on Cu(100) in the far infrared. *Phys. Rev. Lett.* **1990**, *65*, 480−483.
(84) Cox, D. F.; Schulz, K. H. Interaction of CO with Cu^+ cations: CO adsorption on Cu_2O (100). *Surf. Sci.* **1991**, *249*, 138−148.
(85) Reyter, D.; Odziemkowski, M.; Bélanger, D.; Roué, L. Electrochemically Activated Copper Electrodes Surface Characterization, Electrochemical Behavior, and Properties for the Electroreduction of Nitrate. *J. Electrochem. Soc.* **2007**, *154*, K36−K44.
(86) Wang, X.; Andrews, L. Infrared Spectra and Structures of the Coinage Metal Dihydroxide Molecules. *Inorg. Chem.* **2005**, *44*, 9076−9083.
(87) Liu, L. Z.; Wu, X. L.; Gao, F.; Shen, J. C.; Li, T. H.; Chu, P. K. Determination of surface oxygen vacancy position in SnO_2 nanocrystals by Raman spectroscopy. *Solid State Commun.* **2011**, *151*, 811−814.
(88) Yu, K. N.; Xiong, Y. H.; Liu, Y. L.; Xiong, C. S. Microstructural Change of Nano-SnO_2 Grain Assemblages with the Annealing Temperature. *Phys. Rev. B: Condens. Matter Mater. Phys.* **1997**, *55*, 2666.
(89) Shek, C. H.; Lin, G. M.; Lai, J. K. L. Effect of Oxygen Deficiency on the Raman Spectra and Hyperfine Interactions of Nanometer SnO_2. *Nanostruct. Mater.* **1999**, *11*, 831−835.
(90) Meier, C.; Lüttjohann, S.; Kravets, V. G.; Nienhaus, H.; Lorke, A.; Ifeacho, P.; Wiggers, H.; Schulz, C.; Kennedy, M. K.; Kruis, F. E. Vibrational and Defect States in SnO_x Nanoparticles. *J. Appl. Phys.* **2006**, *99*, 113108.
(91) Sexton, B. A. Vibrational Spectrum of Carbon Monoxide Chemisorbed on a Copper(100) Surface. *Chem. Phys. Lett.* **1979**, *63*, 451−454.
(92) Davis, A. R.; Oliver, B. G. A Vibrational-Spectroscopic Study of the Species Present in the CO_2-H_2O System. *J. Solution Chem.* **1972**, *1*, 329−339.
(93) Kepp, K. P. A Quantitative Scale of Oxophilicity and Thiophilicity. *Inorg. Chem.* **2016**, *55*, 9461−9470.
(94) Schouten, K. J. P.; Pérez Gallent, E.; Koper, M. T. M. Structure Sensitivity of the Electrochemical Reduction of Carbon Monoxide on Copper Single Crystals. *ACS Catal.* **2013**, *3*, 1292−1295.
(95) Calle-Vallejo, F.; Koper, M. T. Theoretical Considerations on the Electroreduction of CO to C_2 Species on Cu(100) Electrodes. *Angew. Chem., Int. Ed.* **2013**, *52*, 7282−7285.

DOI: 10.1021/acscatal.9b04368
ACS Catal. 2020, 10, 672−682